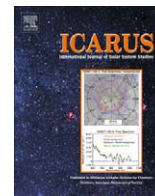




Contents lists available at ScienceDirect

Icarus

journal homepage: [www.elsevier.com/locate/icarus](http://www.elsevier.com/locate/icarus)

## Further observations of regional dust storms and baroclinic eddies in the northern hemisphere of Mars

David P. Hinson<sup>a,b,\*</sup>, Huiqun Wang<sup>c</sup><sup>a</sup> Carl Sagan Center, SETI Institute, 515 N. Whisman Rd., Mountain View, CA 94043, USA<sup>b</sup> Department of Electrical Engineering, Stanford University, 350 Serra Mall, Stanford, CA 94305, USA<sup>c</sup> Atomic and Molecular Physics Division, Smithsonian Astrophysical Observatory, 60 Garden St., Cambridge, MA 02138, USA

## ARTICLE INFO

## Article history:

Received 24 April 2009

Revised 22 August 2009

Accepted 24 August 2009

Available online xxxx

## Keywords:

Mars, Atmosphere

Mars, Climate

Atmospheres, Dynamics

## ABSTRACT

We have investigated the near-surface meteorology in the northern hemisphere of Mars through detailed analysis of data obtained with Mars Global Surveyor in January–August 2005. The season in the northern hemisphere ranged from midsummer through winter solstice of Mars Year (MY) 27. We examined composite, wide-angle images from the Mars Orbiter Camera and compiled a catalog of the dust storms that occurred in this interval. As in previous martian years, activity in the northern hemisphere was dominated by regional “flushing” dust storms that sweep southward through the major topographic basins, most frequently in Acidalia Planitia. We also used atmospheric profiles retrieved from radio occultation experiments to characterize eddy activity near the surface at high northern latitudes. There are strong correlations between the two sets of observations, which allowed us to identify three factors that influence the timing and location of the regional dust storms: (1) transitions among baroclinic wave modes, which strongly modulate the intensity of meridional winds near the surface, (2) storms zones, which impose strong zonal variations on the amplitude of some baroclinic eddies, and (3) stationary waves, which further modulate the wind field near the surface. The flushing dust storms ceased abruptly in midautumn, possibly in response to source depletion, CO<sub>2</sub> condensation, a shift in the period of the baroclinic eddies, and changes in the tidal wind field near the surface. Our results extend the meteorological record of the northern hemisphere, substantiate the findings of previous investigations, and further illuminate the climatic impact of baroclinic eddies.

© 2009 Elsevier Inc. All rights reserved.

## 1. Introduction

This paper reports new results concerning two important aspects of the weather in the northern hemisphere of Mars: baroclinic eddies and regional dust storms. We have characterized these phenomena through coordinated analysis of composite images and radio occultation data from Mars Global Surveyor (MGS). These two sets of observations are highly complementary in their sensitivity to diverse aspects of martian meteorology.

This investigation builds on a foundation of knowledge assembled in numerous previous studies. Meteorological data from the Viking Landers revealed that eastward-traveling baroclinic eddies dominate the dynamics near the surface at high northern latitudes during autumn, winter, and spring (e.g. Ryan et al., 1978; Leovy, 1979; Barnes, 1980, 1981; Leovy et al., 1985; James, 1985; Zurek et al., 1992; Collins et al., 1996). These martian weather systems have a characteristic spatial scale of several thousand kilometers,

a remarkable degree of spatial and temporal coherence, and winds sufficient to initiate dust storms.

Further observations of baroclinic eddies were acquired when MGS attained a nearly-circular, polar orbit and began remote sensing of the atmosphere. The Thermal Emission Spectrometer (TES) monitored atmospheric temperatures, dust, clouds, and water vapor with essentially complete global coverage over a span of about 3 martian years (e.g. Smith, 2004). TES temperature profiles have been analyzed extensively to map the spatial structure and seasonal evolution of baroclinic eddies as well as an assortment of other atmospheric waves (Wilson et al., 2002; Hinson et al., 2003; Banfield et al., 2003, 2004; Wang et al., 2005; Wang, 2007).

Radio occultation experiments were also conducted routinely as part of the MGS radio science (RS) investigation (e.g. Hinson et al., 1999). Although their latitude coverage is limited, the RS measurements offer valuable insight into the behavior of baroclinic eddies for two reasons. First, the RS results include accurate measurements of geopotential height on surfaces of constant pressure, which yield unique information about meridional winds near the surface (Hinson, 2006, Figs. 5 and 6). Second, the temperature perturbations and eddy heat flux are confined to a shallow layer near

\* Corresponding author. Address: Carl Sagan Center, SETI Institute, 515 N. Whisman Rd., Mountain View, CA 94043, USA. Fax: +1 650 9617099.

E-mail address: [dhinson@seti.org](mailto:dhinson@seti.org) (D.P. Hinson).

the surface (Hinson, 2006, Figs. 8–10), which is resolved far better by radio occultation than by infrared sounding. These characteristics of the temperature field and meridional heat flux are consistent with eddies that arise from baroclinic instability (e.g. Gill, 1982; Barnes, 1984), in which the disturbance extracts available potential energy from the zonal-mean basic state.

The MGS Mars Orbiter Camera (MOC) has provided extensive observations of a distinctive type of dust storm that occurs in the major topographic basins of the northern hemisphere during autumn and winter (Cantor et al., 2001; Wang et al., 2003, 2005; Cantor, 2007; Wang, 2007). These storms originate through lifting and advection of dust by baroclinic eddies at high northern latitudes. On some occasions these “frontal” storms spread southward as dust is entrained into the near-surface winds of the Hadley circulation, and the resulting “flushing” or “cross-equatorial” storm can progress from high northern latitudes into the tropics in a span of a few days. The diurnally-varying, near-surface winds associated with thermal tides and topographic circulations appear to play an important role in the transition between the frontal and flushing stages of these dust storms (Wang et al., 2003; Wilson et al., 2006).

Essential features of these flushing dust storms have been determined through analysis of MOC images and TES temperature measurements spanning several martian years (Wang et al., 2003, 2005; Wang, 2007). These storms occur more commonly in Acidalia than in Utopia or Arcadia (e.g. Wang et al., 2005), although Utopia was the locus of activity in autumn of Mars Year (MY) 26 (Wang, 2007). (In assigning numbers to martian years we adopt the convention that MY 1 began on 11 April 1955 (Clancy et al., 2000), at the vernal equinox in the northern hemisphere of Mars.) The dust-storm distribution is clearly influenced by a zonal asymmetry in the baroclinic eddies, which appears in the form of a longitude band where the eddy amplitude is significantly larger than the zonal average (e.g. Wang et al., 2005, Fig. 10). This phenomenon, known as a “storm zone” (Hollingsworth et al., 1996), appears most commonly though intermittently near 280°E, to the northeast of Alba Mons and to the northwest of Acidalia Planitia (e.g. Banfield et al., 2004; Wang et al., 2005).

Sequences of flushing dust storms generally appear within two distinct seasonal windows, one in midautumn and the other in midwinter, separated by a lull near winter solstice (e.g. Wang, 2007, Fig. 1). This pattern of dust-storm activity is correlated with seasonal variations in the amplitude and zonal wave number of baroclinic eddies near the surface (e.g. Wang et al., 2005, Fig. 8), which strongly modulate the intensity of meridional winds near the surface (Hinson, 2006, Fig. 6). Flushing dust storms occur commonly, though not exclusively, in connection with wave-3 baroclinic eddies with periods of 2–3 sols. These conclusions are supported by several years of observations (Wang et al., 2005; Wang, 2007) as well as numerical simulations with a Mars General

Circulation Model (MGCM) (Wang et al., 2003; Wilson et al., 2006; Basu et al., 2006).

The impact of a flushing dust storm is accentuated by its coupling with the Hadley circulation, which can result in rapid changes in dust opacity and thermal structure on a global scale (e.g. Cantor et al., 2001; Wang et al., 2003; Cantor, 2007; Wang, 2007). In this way a sequence of cross-equatorial dust storms can trigger an appreciable change in the global state of the atmosphere, as indicated by the sudden appearance of a planet-encircling haze and a characteristic intensification of the Hadley circulation. This type of event has been observed during midautumn and midwinter of many martian years (e.g. Cantor et al., 2001; Wang et al., 2003; Liu et al., 2003; Smith, 2004, 2009; Cantor, 2007; Wang, 2007), and MGCMs have made significant progress in simulating the initiation and development of this type of dust storm (e.g. Wang et al., 2003; Wilson et al., 2006; Basu et al., 2006).

In this paper we extend the existing record of weather in the northern hemisphere through analysis of MGS data obtained during January–August 2005, part of its final martian year of operations. This interval corresponds to midsummer through winter solstice of MY 27. We use a combination of MOC composite images and RS atmospheric profiles to investigate key atmospheric phenomena, including both flushing dust storms and baroclinic eddies. This is the first detailed examination of martian meteorology in this period.

The MOC observations from MY 24–26 have been analyzed extensively (e.g. Cantor et al., 2001; Wang and Ingersoll, 2002; Wang et al., 2003, 2005; Cantor, 2007; Wang, 2007), but the subset of data considered here has received little attention. Section 2 reviews basic features of these data and the procedure used in constructing composite images. Section 3 shows a selection of images and describes the regional dust storms that occurred in the northern hemisphere during autumn of MY 27, building on the initial results reported by Cantor (2007, Section 5.7).

The RS instrument on MGS was the only atmospheric sounder in operation during autumn of MY 27. As with the MOC images, the RS data from MY 24–26 have received considerably more attention (e.g. Hinson and Wilson, 2002, 2004; Hinson et al., 2003; Hinson, 2006) than the subset of data considered here. Section 4 reviews the properties of the retrieved atmospheric profiles and the spatial coverage of these experiments. Section 5 describes our method of space–time analysis and applies it to these data, yielding a unique characterization of the eddies that appear near the surface at high northern latitudes. These results are consistent with the preliminary findings of Hinson and Wang (2008) but far more complete.

Martian baroclinic eddies undergo distinctive transitions in their period and zonal wave number (e.g. Collins et al., 1996; Hinson, 2006; Hinson and Wang, 2008). Section 5 devotes con-

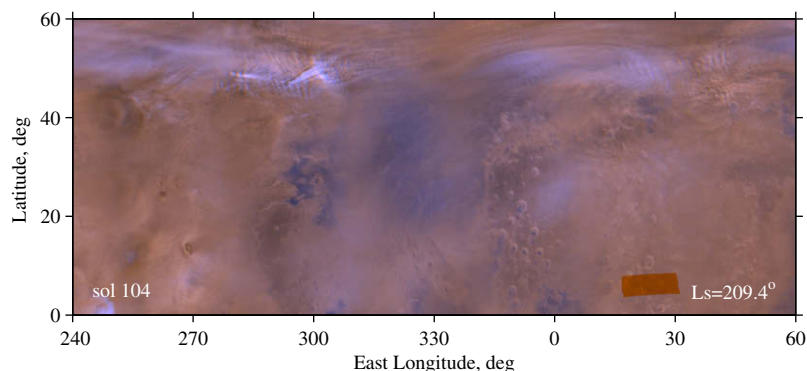


**Fig. 1.** The appearance of the Acidalia and Chryse basins as observed by the MGS MOC WA cameras during an interlude between regional dust storms. Values of  $L_s$  and sol number are indicated in the lower corners. Diffuse dust and condensate clouds are present poleward of about 45°N.

siderable attention to this phenomenon and its consequences, while also examining the meridional winds near the surface and the characteristics of storm zones and stationary waves. These results provide new insight into the factors that control the timing and location of regional dust storms in the northern hemisphere.

Section 6 discusses selected results and their relationship to previous work. In particular, Section 6.1 describes key similarities and differences relative to midautumn dust storms of previous years. The flushing dust storms ceased abruptly in midautumn of MY 27, and Section 6.4 offers several possible explanations.

Before proceeding, we review conventions for time keeping on Mars. The term sol denotes the mean solar day of 88,775 s. Local time is expressed in true solar hours (24 per sol). The areocentric longitude of the Sun,  $L_s$ , measures the seasons on Mars, with  $L_s \equiv 0^\circ$  at the vernal equinox of the northern hemisphere. We also define the sol number as an integer that increments as the prime meridian crosses midnight, with the counter set to 1 at  $L_s = 150^\circ$  of MY 27.

## 2. Observations of the atmosphere by the MGS MOC

The MGS MOC included a pair of wide-angle (WA) cameras designed for systematic global monitoring of the martian atmosphere and surface (e.g. Malin et al., 1992; Cantor et al., 2001). Each WA camera covers a different wavelength band, one at 575–625 nm (red) and the other at 400–450 nm (blue). Owing to this complementary spectral coverage, it is often possible to discriminate between atmospheric dust, which appears brighter when viewed with the red filter, and condensate clouds, which appear brighter in observations with the blue filter (e.g. James, 1985; Cantor et al., 2001; Wang and Ingersoll, 2002).<sup>1</sup>

Throughout its primary and several extended missions, MGS remained in a nearly-circular, sun synchronous, polar orbit. The equator crossing on the dayside occurred at a local time of about 14 h, with the spacecraft traveling from south to north. Both WA cameras routinely monitored the atmosphere and surface in a “daily global map” mode, yielding “push-broom” image swaths that extend along track from pole to pole and across track from limb to limb, with a uniform resolution in most cases of 7.5 km per pixel (e.g. Cantor et al., 2001; Wang and Ingersoll, 2002; Cantor, 2007). Cantor et al. (2001) exploited the uniform daily global coverage of the WA images to conduct the first definitive survey of martian dust storms. Subsequent studies have yielded enormous advances in our understanding of the seasonal and spatial distributions of dust storms and their impact on climate (e.g. Wang et al., 2003, 2005; Strausberg et al., 2005; Cantor et al., 2006; Cantor, 2007; Wang, 2007).

The images used in this investigation take the form of Mars Daily Global Maps (MDGMs), which were assembled from groups of contiguous WA swaths using the procedure described by Wang and Ingersoll (2002). The steps of processing required to transform a set of raw images into a MDGM include correction for irregularities in the camera response, photometric calibration to compensate for variations in viewing geometry, and projection of individual swaths into a composite global map. The MDGMs distill the information from the raw WA swaths into a standardized, intelligible data product that can be used directly for investigations of atmospheric aerosols and related meteorology (e.g. Cantor et al., 2001; Wang and Ingersoll, 2002; Wang et al., 2003, 2005; Cantor, 2007; Wang, 2007).

<sup>1</sup> For interpretation of color in Figs. 1–8 and 11, the reader is referred to the web version of this article.

## 3. Regional dust storms in the northern hemisphere

Cantor (2007, Section 5.7) noted that several cross-equatorial dust storms occurred in the northern hemisphere during autumn of MY 27, but the discussion is brief and restricted to information available from MOC images alone. In this section we describe this series of dust storms in greater detail, assembling a catalog of basic dust-storm properties through examination of MDGMs. The results provide a basis for comparisons with independent observations of atmospheric dynamics in Section 5.

We did not attempt to measure their size, but it appears that most of the events discussed here would qualify as regional dust storms, which are defined by Cantor et al. (2001) to have an area of at least  $1.6 \times 10^6$  km<sup>2</sup> and a minimum duration of 2 sols. During autumn of MY 27, these dust storms appeared more frequently in Acidalia Planitia than in the other major topographic basins of the northern hemisphere, and we therefore focus primarily on activity within that region.

### 3.1. Context

Fig. 1 shows a portion of a “color” composite MDGM constructed from WA images in the red and blue wavelength bands.<sup>1</sup> This equatorial map (in simple cylindrical equidistant projection) covers longitudes of 120°W to 60°E and latitudes from the equator to 60°N, a region roughly centered on Acidalia Planitia (330°E, 40°N) and Chryse Planitia (320°E, 25°N). The outflow channel of Kasei Valles appears as a low albedo feature at 300°E, 27°N, with Sharonov Crater at its center. By showing the appearance of this region at a time in early autumn when the atmosphere is relatively clear, Fig. 1 provides a visual context for evaluating subsequent images of dust storms.

Fig. 2 shows the surface elevation of the same region, as derived from measurements by the MGS Mars Orbiter Laser Altimeter (MOLA) (Smith et al., 2001). This map characterizes the topographic setting for the regional dust storms, while highlighting prominent features that are easily overlooked in Fig. 1, such as Alba Mons (250°E, 40°N) and Ascreaus Mons (255°E, 11°N).

### 3.2. Image processing

The spatial extent of a dust storm is sometimes ambiguous in an isolated MDGM, particularly if its outer boundaries are not sharp or if surrounding surface features are partially obscured by diffuse haze. The presence of subtle photometric artifacts in the MDGMs can also cause uncertainty (e.g. Wang and Ingersoll, 2002). We attempted to compensate for this ambiguity through image processing, using a simple technique that accentuates the effect of atmospheric dust.

In this step of the analysis we used only WA images in the red wavelength band, which provides better sensitivity to atmospheric dust than the blue wavelength band (e.g. James, 1985; Cantor et al., 2001; Wang and Ingersoll, 2002). Our procedure for image processing begins with a pair of red-filter MDGMs, one that contains a dust storm and another where the atmosphere is relatively clear. The pair of images is combined to produce a hybrid MDGM:

$$I_H = I_D + (I_D - I_R) = 2 \times I_D - I_R, \quad (1)$$

where  $I_D$  is the dust storm image,  $I_R$  is the “clear” reference image, and  $I_H$  is the resulting hybrid. The formula is applied at each latitude–longitude grid point within the MDGM. At locations outside the boundaries of a dust storm,  $I_D$  and  $I_R$  are essentially the same, so that Eq. (1) has little effect on the appearance of the martian surface. However, a dust storm is generally brighter than an ice-free

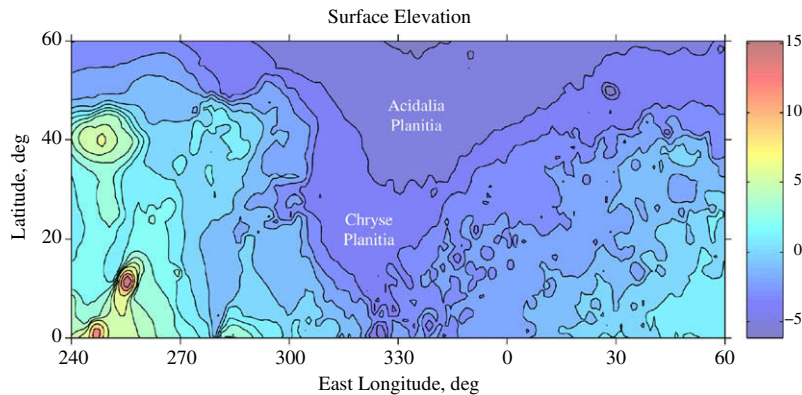


**Fig. 2.** Map of surface elevation derived from measurements by the MGS MOLA (Smith et al., 2001). The elevation (in kilometers) is indicated by color shading as well as contours. The contour levels range from  $-5$  km to  $+15$  km, with a separation of 1 km at elevations below  $+6$  km, increasing to 3 km at higher elevations.

surface, and Eq. (1) accentuates this effect, roughly doubling the contrast associated with a dust storm.

To be effective, a reference image should be free of serious gaps, with no active dust storms in the region of interest. The quality of a hybrid image generally improves when the spacecraft crossed the equator at about the same longitudes for both  $I_D$  and  $I_R$ , so that any seams in the images are nearly aligned. In all subsequent figures, the hybrid image is accompanied by the color MDGM of the dust storm, which provides a complementary characterization of the scene.

### 3.3. Regional dust storms in Acidalia

We now illustrate the characteristic features of a type of regional dust storm that occurred repeatedly in Acidalia during autumn of MY 27. Fig. 3 shows one such event as it appears in color MDGMs, while Fig. 4 shows the hybrid version of the same 2-sol sequence. Hybrid MDGMs allow large-scale dust storms to be iden-

tified and characterized with greater confidence, as demonstrated by comparison of the results in Figs. 3 and 4. This type of processing is particularly effective on sol 113 (lower panels), where both the outer boundaries and internal structure of the dust storm are revealed more clearly in the hybrid version.

The regional dust storm in Figs. 3 and 4 progresses through two stages. On the first day of the sequence (sol 112), a narrow, curving band of dust appears in Acidalia. Judging by its location and its resemblance in shape and scale to a cold front, it is probably associated with a baroclinic eddy (e.g. Wang et al., 2003), and we will therefore refer to this type of event as a frontal dust storm. By sol 113, the dust storm has spread southward from Acidalia into Chryse, and it is accompanied by a distinctive linear band of dust that extends for several thousand kilometers to the northeast, roughly from  $330^\circ\text{E}$ ,  $30^\circ\text{N}$  to  $60^\circ\text{E}$ ,  $55^\circ\text{N}$ . We will refer to this second phase of activity as a flushing dust storm.

At its western and southern boundaries, the outline of the flushing dust storm in the lower panel of Fig. 4 roughly conforms with a

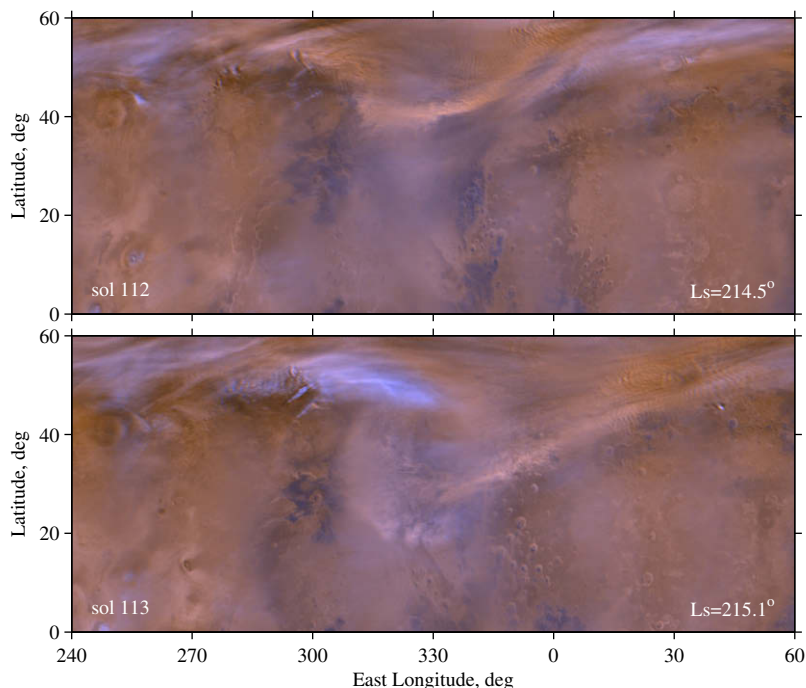


**Fig. 3.** Color MDGMs from two consecutive sols showing the development of a regional dust storm near  $L_s = 215^\circ$  of MY 27. The format is the same as in Fig. 1. (top) A well defined frontal dust storm appears in Acidalia at  $310\text{--}350^\circ\text{E}$ ,  $40\text{--}50^\circ\text{N}$ . (bottom) A flushing dust storm extends from Acidalia into Chryse. Its southern edge is near  $20^\circ\text{N}$ .

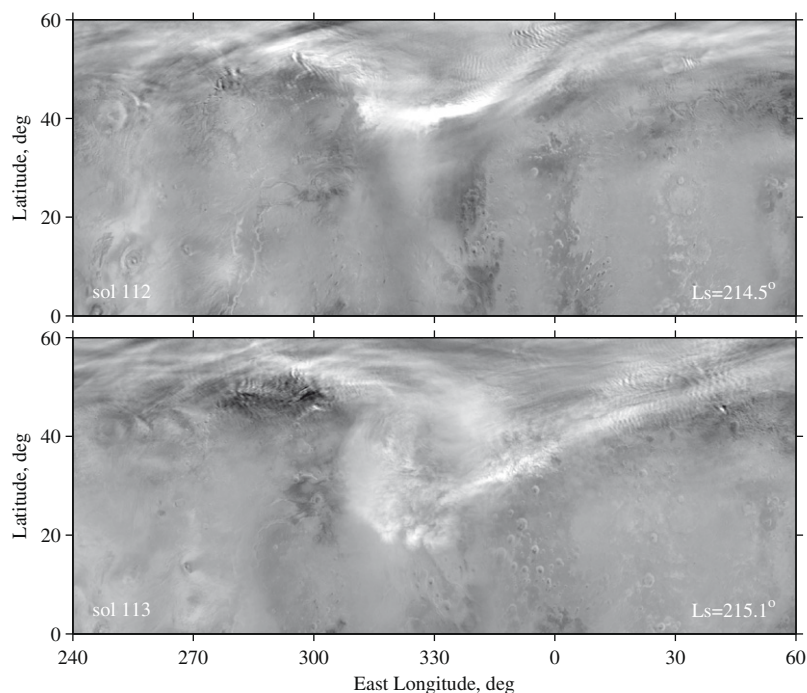


**Fig. 4.** Alternate view of the dust storm sequence in Fig. 3. Each panel shows a hybrid MDGM in which the effects of atmospheric dust have been enhanced through image processing, as described in Eq. (1) and the surrounding text. This pair of hybrids was constructed using reference images from (top) sol 99 and (bottom) sol 104.

contour of constant surface elevation passing through Chryse Planitia (see Fig. 2). This reflects the influence of surface topography on the evolution of the dust storm. In the following 2 sols (not shown), the storm spread along two routes of low elevation, traveling eastward into the outflow channel of Kasei Valles and southward past Chryse.

This type of frontal/flushing dust storm was observed previously in Acidalia during midautumn of MY 24, as discussed by Cantor et al. (2001, Figs. 10 and 11) and Wang et al. (2003, Fig. 1). Similar events recur seasonally in both midautumn and midwinter in all three major basins of the northern hemisphere (Cantor et al., 2001; Wang et al., 2003, 2005; Cantor, 2007; Wang, 2007). However, the series of Acidalia storms that occurred in autumn of MY 27 culminates in an unusual, cyclic sequence of vigorous events, which began about 10 sols after the observations in Fig. 4. We now examine a 4-sol sequence of MDGMs from within this period.

The sequence begins on sol 127 ( $L_s = 224.0^\circ$ ). A broad lobe of dust with a curving southern boundary covers much of Acidalia, as shown in Fig. 5. It has the general appearance of a frontal dust storm, although it is not as narrowly confined as the example in the top panel of Fig. 4. Diffuse haze is also present in the northern tropics at  $310\text{--}330^\circ\text{E}$ , a vestige of dust storms on previous sols.

The frontal dust storm of sol 127 is followed by a flushing dust storm on sol 128 ( $L_s = 224.6^\circ$ ), as shown in Fig. 6. Its spatial structure is similar to the flushing storm in the bottom panel of Fig. 4, but the storm on sol 128 covers a larger area, extending southward into Xanthe Terra ( $310^\circ\text{E}$ ,  $5^\circ\text{N}$ ). In both cases, the flushing storm appears to be confined along its western boundary by the steep rise in surface elevation near  $305^\circ\text{E}$ ,  $10\text{--}50^\circ\text{N}$  (see Fig. 2).

Another pair of frontal/flushing dust storms follows immediately on sols 129 and 130, closely repeating the pattern of the previous 2 sols, as shown in Figs. 7 and 8. Despite dramatic variations from one sol to the next, there is remarkably little difference between the frontal dust storms of sols 127 and 129 or between the flushing dust storms of sols 128 and 130. For example, the outflow channel of Kasei Valles is easy to identify on sols 127 and 129

(Figs. 5 and 7) but is largely obscured by dust on sols 128 and 130 (Figs. 6 and 8).

### 3.4. Spatial and temporal distribution of northern regional dust storms

We examined MDGMs from late summer to winter solstice of MY 27, searching for dust storms of the type shown in Figs. 4–8. We considered three criteria in deciding whether a particular event should be included in this category: (1) it consists of a frontal/flushing sequence with a duration of at least 2 sols, (2) the frontal stage takes the form of a linear band or wave-like arc, with a typical extent of  $20\text{--}30^\circ$  in longitude, and (3) the flushing stage reaches the tropics and covers a substantial area, with typical dimensions of  $20\text{--}30^\circ$  in both longitude and latitude.

We identified 15 events that appear to satisfy these conditions, as listed in Table 1. This type of dust storm was observed in all three of the major topographic basins of the northern hemisphere, but their distribution is not uniform, with significantly more events in Acidalia (9) than in Arcadia (3) or Utopia (3). The shape, orientation, and general visual appearance of these storms also varies significantly with location, and in some cases our attempts to categorize them involved subjective judgments. However, none of our main conclusions hinges on whether any single dust storm is included in or excluded from Table 1.

These regional dust storms began near the autumnal equinox, occurring nearly simultaneously in Acidalia and Utopia at  $L_s = 177\text{--}178^\circ$  and again 10 sols later at  $L_s = 182\text{--}183^\circ$ . The second pair of storms is particularly weak. The frontal stage in both pairs of storms has a distinct, wave-2 zonal structure. This activity was followed by a relatively quiet period lasting more than 30 sols, which ended with a substantial storm in Acidalia at  $L_s = 203.8^\circ$ .

Regional dust storms occurred frequently in midautumn, at  $L_s = 215\text{--}226^\circ$ , then ceased abruptly. Fig. 4 shows the first in this series of storms. Near the end of this interval, Acidalia experienced a cyclic pattern of intense activity, as shown in Figs. 5–8, compris-

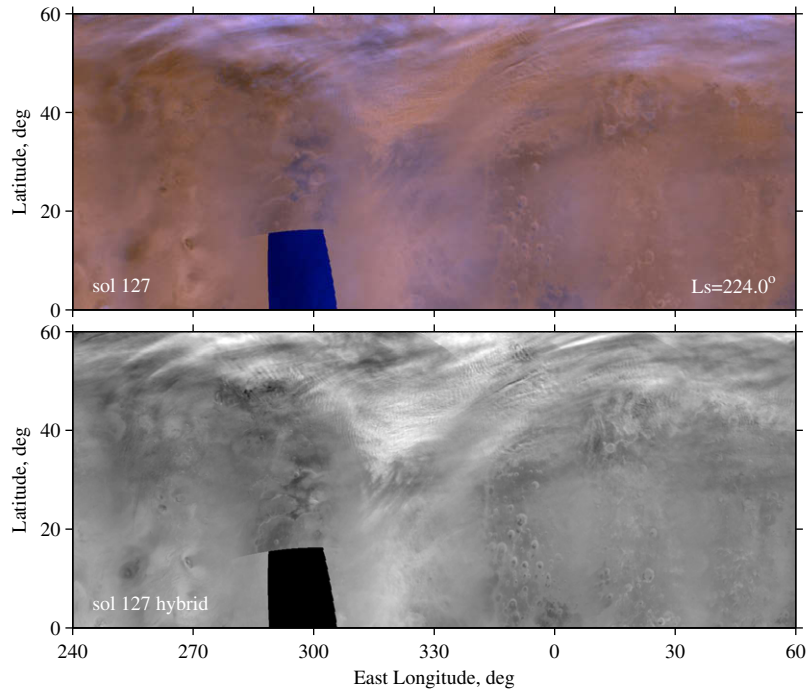


**Fig. 5.** Observations on sol 127 ( $L_s = 224.0^\circ$ ) of a diffuse frontal dust storm centered at about  $45^\circ\text{N}$  in Acidalia. The two panels show (top) a quadrant of the equatorial, color MDGM, and (bottom) the corresponding hybrid MDGM constructed with a reference image from sol 136. A similar dust storm occurred two sols later, as shown in Fig. 7.

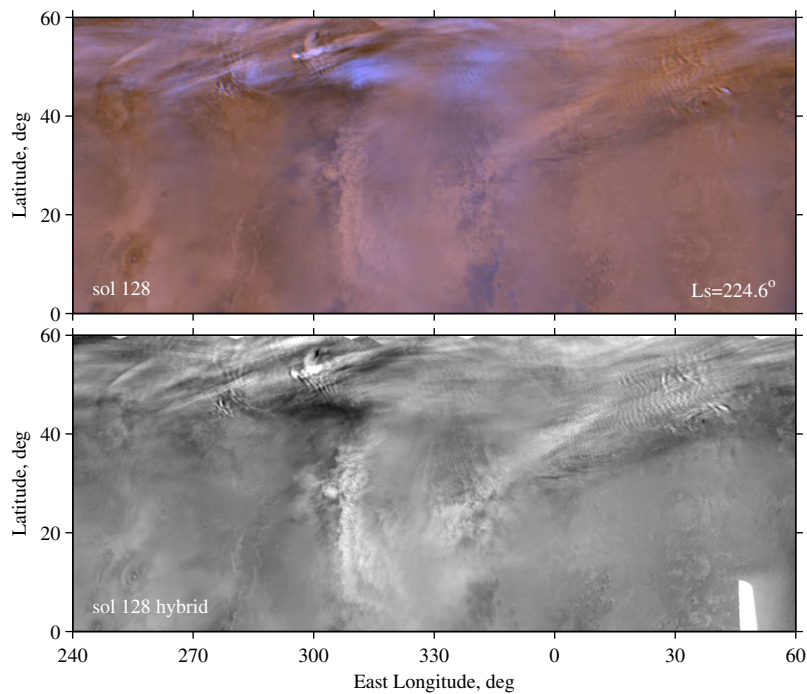


**Fig. 6.** Observations on sol 128 ( $L_s = 224.6^\circ$ ) of a broad flushing dust storm that extends from Acidalia, across Chryse, and into Xanthe Terra. The two panels show (top) a quadrant of the equatorial, color MDGM, and (bottom) the corresponding hybrid MDGM constructed with a reference image from sol 145. A similar dust storm occurred two sols later, as shown in Fig. 8.

ing frontal and flushing storms on alternate sols during  $L_s = 221\text{--}226^\circ$  (sols 123–130).

When compared with analogous events from previous years, the dust storm sequence described here most closely resembles the one observed in autumn of MY 24 (Cantor et al., 2001; Wang et al., 2003). The most striking similarity is the recurrence of a

series of vigorous flushing dust storms in Acidalia at about  $L_s = 221\text{--}225^\circ$  (Cantor et al., 2001, Section 6.6). Nonetheless, the storm sequence within this seasonal window of MY 27 is more cyclic in nature than its counterpart of MY 24. We defer further comparison between the events of the two years to Section 6.1.

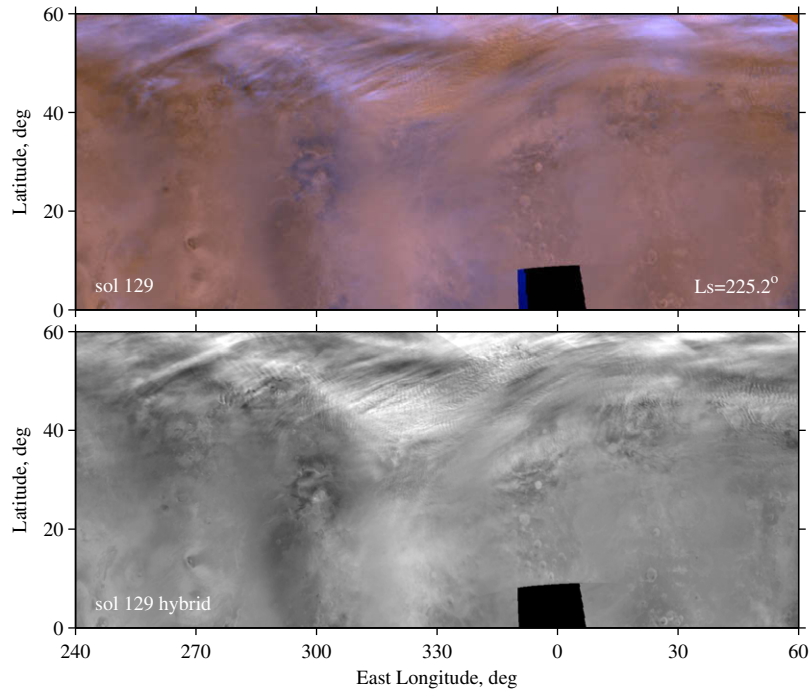


**Fig. 7.** Observations on sol 129 ( $L_s = 225.2^\circ$ ) of a diffuse frontal dust storm centered at about  $45^\circ\text{N}$  in Acidalia. The two panels show (top) a quadrant of the equatorial, color MDGM, and (bottom) the corresponding hybrid MDGM constructed with a reference image from sol 136. A similar dust storm occurred two sols earlier, as shown in Fig. 5.

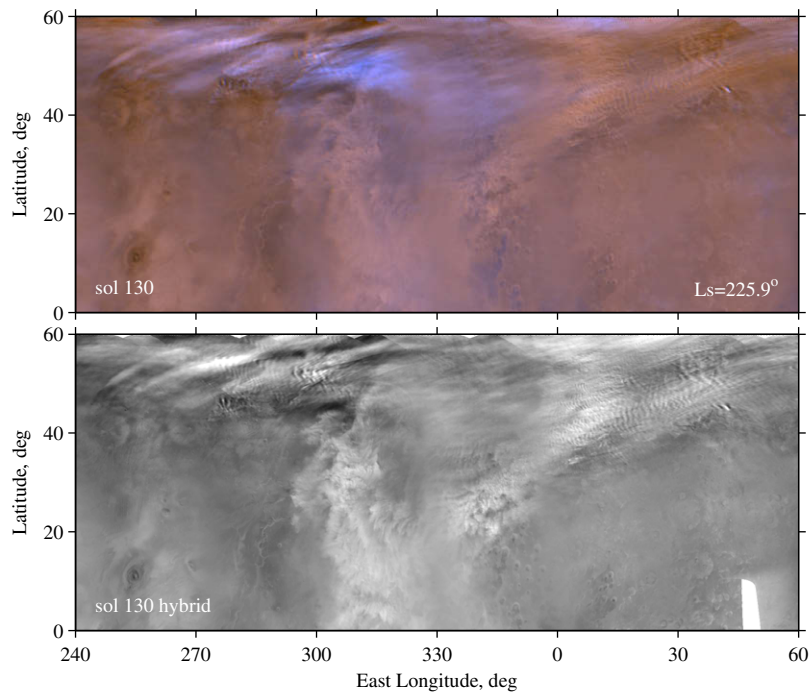


**Fig. 8.** Observations on sol 130 ( $L_s = 225.9^\circ$ ) of a broad flushing dust storm that extends from Acidalia, through Chryse, and across the equator. The two panels show (top) a quadrant of the equatorial, color MDGM, and (bottom) the corresponding hybrid MDGM constructed with a reference image from sol 145. A similar dust storm occurred two sols earlier, as shown in Fig. 6.

#### 4. Atmospheric sounding through radio occultation

The preceding section used MOC MDGMs to characterize the regional dust storms of the northern hemisphere. We now expand the discussion to include the meteorological context in which they occurred.

MGS performed radio occultation experiments from January 1998 to September 2006, a span of about 4.6 martian years. Each experiment yields a profile of pressure  $p$  and temperature  $T$  versus radius and geopotential height  $Z$  that extends from the surface to the 10-Pa pressure level (Hinson et al., 1999), corresponding to an altitude of about 40 km in the tropics. The uncertainties in  $p$

**Table 1**  
Regional dust storms of the northern hemisphere.

$L_s$ (°)	Sol number	Location	
177.3	51		Utopia
177.6	51	Acidalia	
182.8	60	Acidalia	
183.1	61		Utopia
203.8	95	Acidalia	
215.1	113	Acidalia	
215.3	114	Arcadia	
218.0	118		Utopia
220.1	121	Acidalia	
221.7	124	Arcadia	
222.0	124	Acidalia	
223.3	126	Acidalia	
224.6	128	Acidalia	
225.9	130	Acidalia	
226.2	131	Arcadia	

Note: This list includes dust storms of the type shown in Figs. 3–8 that occurred between late summer and winter solstice of MY 27. The time assigned to each event refers to the MOC WA swath that contains the flushing stage of the storm. Sols are counted from  $L_s = 150^\circ$  of MY 27.

and  $T$  vary strongly with pressure, decreasing from about 5% at 10 Pa to about 0.3% at 610 Pa, near the surface.

The MGS occultations were sounding the atmosphere at high northern latitudes during all of the regional dust storms listed in Table 1. About 2400 RS profiles were obtained between midsummer and winter solstice of MY 27, a span of 230 sols. We will use these RS observations to characterize the dynamics near the surface and to investigate their influence on the timing and location of the regional dust storms.

Fig. 9 summarizes important features of these RS observations. The top panel shows samples of  $Z_{610}$ , the geopotential height at 610 Pa. The middle panel shows the corresponding measurements of temperature,  $T_{610}$ . Both sets of observations are characterized by large fluctuations on time scales of less than 1 sol superimposed on

a seasonally varying mean value. The seasonal trend in  $Z_{610}$  arises primarily from sublimation of  $\text{CO}_2$  at the south pole, which causes  $Z_{610}$  to increase by about 1.5 km between  $L_s = 160^\circ$  and  $L_s = 260^\circ$ . The mean temperature decreases by about 40 K during the same interval. The temperature minima occasionally dip below  $\text{CO}_2$  saturation (147.7 K at 610 Pa), but seldom by more than 2 K.

As we will show in Section 5, a combination of baroclinic eddies and stationary waves is responsible for the large dynamical fluctuations in  $Z_{610}$  and  $T_{610}$ , whose amplitude sometimes exceeds 500 m and 10 K, respectively. The measurement uncertainties in  $Z_{610}$  and  $T_{610}$ , about 20 m and 0.4 K, respectively, for this subset of data, are barely discernible on the scale of Fig. 9.

The latitude of the RS measurements ranges from about  $79^\circ\text{N}$  at  $L_s = 160^\circ$  to about  $65^\circ\text{N}$  at  $L_s = 220^\circ$ , as shown in Fig. 9. The average surface elevation within this latitude band is about  $-4$  km. The local time of the RS measurements drifted from 6 h at  $L_s = 140^\circ$  to about 15 h at  $L_s = 260^\circ$ , a net change of 9 h in a span of 230 sols.

In the interval considered here, radio occultation experiments were conducted on about five out of six MGS orbits. The data gaps are generally short, seldom exceeding three orbits, with only one notable exception. No data were recorded during a 16-orbit (1.3-sol) interval centered on  $L_s = 198.5^\circ$ , owing to a rare problem with automated data collection at the NASA Deep Space Network (DSN). On the other hand, data gaps were entirely absent from a remarkable string of experiments conducted on 144 consecutive orbits at  $L_s = 217\text{--}224^\circ$ .

## 5. Atmospheric dynamics near the surface

We will characterize the eddy activity within the lowest scale height above the surface through analysis of the RS measurements of  $Z_{610}$  that appear in Fig. 9. The information content of data such as these is well understood (e.g. Chapman et al., 1974; Salby, 1982; Lait and Stanford, 1988; Wu et al., 1995), owing to the long heritage of atmospheric sounding from satellites in polar orbit. We

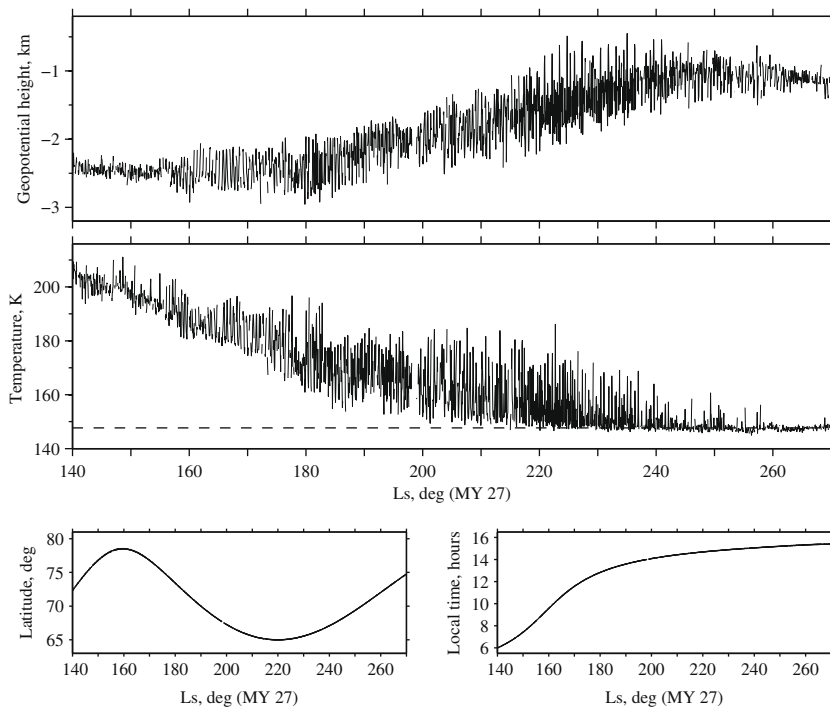


**Fig. 9.** Measurements at 610 Pa of (top) geopotential height and (middle) temperature in the interval between midsummer and winter solstice of MY 27. Lines connect observations from successive orbits, which are separated in time by about 0.08 sols. The dashed line in the middle panel is the saturation temperature of  $\text{CO}_2$  at 610 Pa. The other panels show the coverage of the measurements in (lower left) latitude and (lower right) local time.

are building on the results of a previous investigation (Hinson, 2006) by applying the same method of analysis to additional RS data.

### 5.1. Space–time analysis

The latitude of these RS observations remains essentially constant from sol to sol, while the measurement longitude moves steadily westward as Mars rotates beneath the sun-synchronous polar orbit of MGS. Observations from consecutive orbits are separated in time by about 0.08 sols and in longitude by about 29°. This type of space–time sampling can be used to constrain the temporal variations and zonal structure of atmospheric eddies, but the systematic dependence of the measurement longitude on the time of observation limits the information content of these data.

As in previous work (Hinson, 2006), we characterized the oscillations in  $Z_{610}$  about the seasonal trend through least squares analysis. This approach relies on a simple model for a periodic atmospheric wave:

$$Z' \equiv A \cos(2\pi f t_u - \epsilon). \quad (2)$$

Here,  $t_u$  is universal time (on Mars). Three parameters describe the wave: the amplitude  $A$ , the frequency  $f$ , and the phase  $\epsilon$ .

A periodogram can be constructed by systematically comparing this model with observations of  $Z_{610}$  (e.g. Press and Teukolsky, 1988; Wu et al., 1995). We begin by selecting a subset of data. (For the data considered here, the optimum span of each subset is about 13 sols, as explained in Section 5.2.) We solve for the seasonal trend  $\bar{Z}$  by fitting a quadratic polynomial to samples of  $Z_{610}$  versus  $t_u$ . We then estimate the harmonic content of the data at a selected value of  $f$  through least squares analysis, obtaining the solutions for  $A$  and  $\epsilon$  that yield the best match between  $Z'$  and the detrended data  $Z_{610} - \bar{Z}$ . This step is repeated for values of  $f$  distributed uniformly across the interval 0–5  $\text{sol}^{-1}$ , with a typical sample spacing of 0.01  $\text{sol}^{-1}$ , sufficient to resolve the spectral peaks. The periodogram displays the solutions for  $A^2$  as a function of  $f$ .

Fig. 10 shows a periodogram computed from a subset of the geopotential data in Fig. 9. Four narrow spectral peaks are largely responsible for the fluctuations of  $Z_{610}$  at 66°N during  $L_s = 230$ – $240^\circ$ . The spectral resolution  $\delta f$  is roughly equal to the inverse of the time span  $\delta t$  of the data subset. In this case,  $\delta t = 15$  sols, so that  $\delta f = 0.07 \text{ sol}^{-1}$ , comparable to the full width at half maximum of each spectral peak in Fig. 10. These four peaks correspond to wave modes with well-defined frequencies, and our method of analysis provides reliable estimates of  $f$ ,  $A$ , and  $\epsilon$  for each mode.

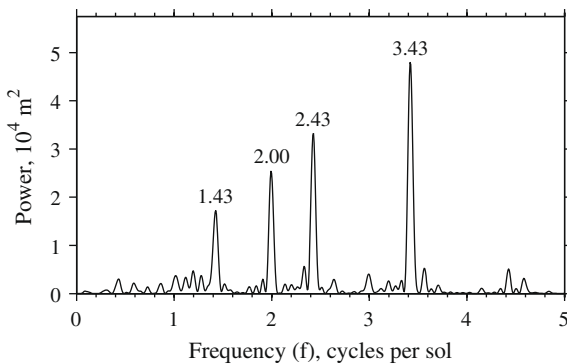


**Fig. 10.** Periodogram of space–time variations in  $Z_{610}$  at 66°N during  $L_s = 230$ – $240^\circ$  of MY 27. The numbers specify the frequency ( $\text{sol}^{-1}$ ) of the four main spectral peaks.

When observed from a sun-synchronous polar orbit, the frequency of an atmospheric wave is Doppler shifted by the rotation of Mars, so that the periodogram measures the combined effects of zonal and temporal variations (e.g. Conrath, 1981; Lait and Stanford, 1988). This can be expressed as

$$f = \sigma + s/\tau, \quad (3)$$

where  $\sigma$  is the wave frequency ( $\text{sol}^{-1}$ ) as observed from a fixed location on the surface,  $s$  is the zonal wave number (dimensionless), and  $\tau$  is the effective rotation period, as discussed below. We adopt sign conventions where  $\sigma > 0$  for a wave traveling eastward and  $s$  is a positive integer. It is more convenient in some cases to refer to the wave period  $P \equiv \sigma^{-1}$ . When expressed in terms of these parameters, the wave model in Eq. (2) becomes (Hinson, 2006):

$$Z' = A \cos(s\lambda - 2\pi\sigma t_u - \psi), \quad (4)$$

where  $\psi$  is the phase (analogous to  $\epsilon$ ), and  $\lambda$  is east longitude.

The slow but steady drift in the local time of the RS data affects the separation in  $\lambda$  between observations on successive orbits. The value of  $\tau$  appropriate to these measurements therefore differs from the mean solar day (1 sol  $\equiv 88,775$  s) by an amount that ranges from about 0.5% at  $L_s = 160^\circ$  to less than 0.2% after  $L_s = 185^\circ$ . However, our solutions for  $s$  and  $\sigma$  are derived through use of Eq. (4), which fully accounts for the drift in local time.

The results in Fig. 10 constrain the values of  $\sigma$  and  $s$  but do not define them uniquely. For example, this type of observation cannot distinguish between a wave-2 disturbance traveling eastward with  $\sigma = +0.3 \text{ sol}^{-1}$  and a wave-3 disturbance traveling westward with  $\sigma = -0.7 \text{ sol}^{-1}$ . Each has a Doppler-shifted frequency  $f = 2.3 \text{ sol}^{-1}$ . This ambiguity is unavoidable for the data considered here, where the latitude of interest is observed only once per spacecraft orbit (e.g. Chapman et al., 1974; Salby, 1982; Lait and Stanford, 1988; Wu et al., 1995).

This ambiguity can be resolved with guidance from previous observations by Viking Lander 2, which yielded two key results (e.g. Ryan et al., 1978; Leovy, 1979; Barnes, 1980; Barnes, 1981; Zurek et al., 1992). First, the relative phasing of variations in pressure and meridional wind speed indicate that the transient eddies travel eastward. Second, the period  $P$  of these eddies, which can be measured unambiguously by an observer at a fixed location on the surface, generally falls within the range of 2–10 sols. In our notation,  $\sigma > 0$  with a magnitude of 0.1–0.5  $\text{sol}^{-1}$ . With these constraints, values for  $s$  and  $\sigma$  can be deduced with confidence from a least squares solution for  $f$ .

The space–time sampling of the data used here also fails to resolve the ambiguity between stationary waves and solar-asynchronous thermal tides (e.g. Hinson et al., 2003; Hinson, 2006). For example, a stationary wave-2 disturbance ( $s = 2$ ,  $\sigma = 0 \text{ sol}^{-1}$ ) appears with the same fundamental frequency,  $f = 2 \text{ sol}^{-1}$ , as the eastward-traveling, wave-1, diurnal Kelvin wave ( $s = 1$ ,  $\sigma = 1 \text{ sol}^{-1}$ ). However, spectral analysis of RS data from a broad range of seasons and latitudes indicates that solar-asynchronous thermal tides have far smaller amplitudes at high northern latitudes than the stationary waves discussed in this paper (e.g. Hinson et al., 2008). Our identification of stationary waves is also confirmed through comparisons with independent measurements from previous years by the MGS TES (Banfield et al., 2003).

We now apply these considerations to the results in Fig. 10. The dominant mode appears at  $f = 3.43 \text{ sol}^{-1}$ , corresponding to an eastward-traveling wave with  $s = 3$ ,  $\sigma = 0.43 \text{ sol}^{-1}$ . Secondary peaks associated with eastward-traveling waves appear at  $f = 2.43 \text{ sol}^{-1}$ , corresponding to  $s = 2$ ,  $\sigma = 0.43 \text{ sol}^{-1}$ , and  $f = 1.43 \text{ sol}^{-1}$ , corresponding to  $s = 1$ ,  $\sigma = 0.43 \text{ sol}^{-1}$ . In addition, the spectrum in Fig. 10 includes a prominent peak at  $f = 2.0 \text{ sol}^{-1}$  that arises from a stationary wave with  $s = 2$ ,  $\sigma = 0$ .

Within the spectral resolution of these observations, the three traveling waves in Fig. 10 have the same value of  $\sigma$ , corresponding to a period of 2.3 sols, but different values of  $s$ . This is the spectral signature of a storm zone (e.g. Banfield et al., 2004, Section 5). Each spectral peak is associated with a basis function whose amplitude is independent of longitude, as in Eq. (4), but the zonal modulation of eddy amplitude can be represented mathematically as a superposition of such idealized waves. As the storm zone remains stationary in longitude, each component of the superposition must have the same value of  $\sigma$ . The effective zonal wave number of the composite waveform is determined by the dominant spectral peak,  $s = 3$  in this case. We will return to this topic in Section 5.4, which examines the spatial structure of a particularly interesting storm zone.

Weather systems exhibit this sort of zonal asymmetry in numerical simulations, which provided the first evidence for the presence of regional storm zones of enhanced eddy activity on Mars (Hollingsworth et al., 1996, 1997). MGS observations subsequently confirmed the existence of storm zones in both the northern and southern hemispheres (e.g. Banfield et al., 2004; Wang et al., 2005). Large-scale topographic features, such as Alba Mons and Hellas Planitia, are responsible for this phenomenon (e.g. Hollingsworth et al., 1996), although there is considerable uncertainty about the specific mechanism by which it occurs.

## 5.2. Eddy properties

We applied least squares spectral analysis to the full set of observations shown in Fig. 9, computing a sequence of periodograms of  $Z_{610}$  from within a sliding  $8^\circ$  window of  $L_s$  (about 13 sols). The number of data samples within each window ranges from 119 to 154, with a median of 139. Fig. 11 shows the results in the form of a spectrogram, which provides a compact summary of the seasonal evolution of dynamics near the surface.

Two factors constrain the length of the data interval used in constructing each periodogram. First, it should be shorter than the coherence time scale of the dominant eddy modes, about 15–20 sols in this set of observations. This upper bound assures that the time resolution of the spectrogram is sufficient to track the characteristic seasonal evolution of the eddy modes. Second, the interval should be longer than the maximum period of the east-

ward-traveling eddies, about 10 sols in this case. This lower bound yields a frequency resolution that is sufficient to distinguish between the long-period traveling eddies and the stationary waves. Our choice of  $8^\circ$  of  $L_s$  (about 13 sols) falls between these two limits.

Fig. 11 covers the frequency range  $f = 0.75\text{--}3.75 \text{ sol}^{-1}$ . There is little activity outside this spectral window (for example, see Fig. 10). Fig. 11 is annotated at intervals of  $0.5 \text{ sol}^{-1}$  in  $f$  to show the corresponding combinations of  $s$  and  $\sigma$  that are consistent with Viking Lander measurements, as discussed in the previous section.

The primary spectral peaks in Fig. 11 fall into two categories. The first component consists with stationary waves, which appear at both  $f = 1 \text{ sol}^{-1}$  ( $s = 1$ ,  $\sigma = 0 \text{ sol}^{-1}$ ) and  $f = 2 \text{ sol}^{-1}$  ( $s = 2$ ,  $\sigma = 0 \text{ sol}^{-1}$ ). The other major spectral features appear at non-integer values of  $f$ , and these correspond to eastward-traveling baroclinic eddies with zonal wave numbers of  $s = 1\text{--}3$  and frequencies in the range of  $\sigma = 0.1\text{--}0.5 \text{ sol}^{-1}$ .

The amplitudes of the stationary waves in Fig. 11 vary significantly with time at 610 Pa. For example, the  $s = 1$  stationary wave is most intense when it first appears in late summer ( $L_s = 160\text{--}175^\circ$ ). This transitory mode has now been observed in late summer at high northern latitudes in four consecutive martian years (Banfield et al., 2003; Hinson, 2006). In contrast, the  $s = 2$  stationary wave is initially weak and achieves its peak amplitude much later, near  $L_s = 226^\circ$ .

The baroclinic eddies in Fig. 11 evolve through a striking sequence of transitions among eastward-traveling modes with different values of  $s$  and  $\sigma$ . This is a fundamental property of martian weather, but it has received little attention subsequent to its discovery by Collins et al. (1996). Each eddy mode persists for a span of about 10–15° of  $L_s$  (15–20 sols), during which the other modes are weak or absent. Within this set of observations the zonal wave number of the dominant baroclinic eddy alternates among  $s = 3$  at  $L_s = 220\text{--}240^\circ$ ,  $s = 2$  at  $L_s = 180\text{--}195^\circ$ , and  $s = 1$  at  $L_s = 175\text{--}185^\circ$ ,  $200\text{--}215^\circ$ , and  $245\text{--}260^\circ$ .

There is a noticeable shift in the frequency of the wave-3 baroclinic eddies near  $L_s = 230^\circ$ , from  $\sigma = 0.49 \text{ sol}^{-1}$  ( $P = 2.0$  sols) before the transition to  $\sigma = 0.43 \text{ sol}^{-1}$  ( $P = 2.3$  sols) afterwards. Throughout each interval the spectral peak at  $s = 3$  is accompanied by secondary peaks at  $s = 2$  and  $s = 1$ , and all have essentially the same value of  $\sigma$ . This indicates the presence of a storm zone, as discussed in Section 5.1. The shift in the frequency of the primary

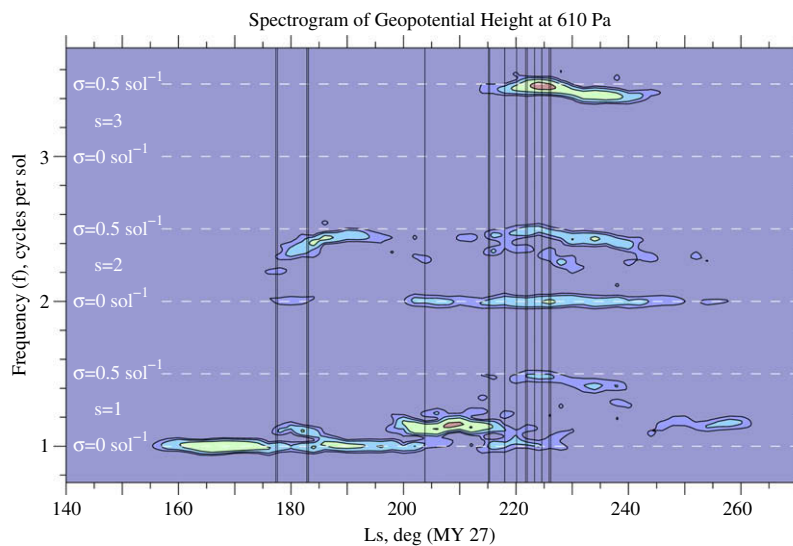


**Fig. 11.** Spectrogram of space–time variations in geopotential height at 610 Pa, showing the seasonal evolution of stationary waves and baroclinic eddies during  $L_s = 140\text{--}270^\circ$  of MY 27. The figure is a composite of periodograms, similar to the one in Fig. 10, computed from within a sliding  $8^\circ$  window of  $L_s$ . Contours are shown at  $0.8$ ,  $1.6$ ,  $3.2$ , and  $6.4 \times 10^4 \text{ m}^2$ , so that each successive contour represents a doubling of power. The vertical lines denote the times of the regional dust storms listed in Table 1.

peak ( $s = 3$ ) at  $L_s = 230^\circ$  is accompanied by a comparable shift in the frequency of the secondary peaks ( $s = 2$  and  $s = 1$ ).

Table 2 summarizes the properties of the most prominent baroclinic eddies during the  $8^\circ$  interval of  $L_s$  in which each mode achieves its peak intensity. The amplitudes listed there refer only to the primary peak in the periodogram. When secondary peaks are also present, as for modes  $d$  and  $e$ , the net amplitude is considerably larger at some longitudes owing to the presence of storm zones. (See Section 5.4 for further discussion.) Each amplitude listed in Table 2 applies to a specific latitude, which drifts gradually with time as shown in Fig. 9, but the meridional structure of the eddies cannot be determined from these observations.

The baroclinic eddies in Table 2 resemble those observed in the northern hemisphere of Mars in previous years (e.g. Wilson et al., 2002; Banfield et al., 2004; Wang et al., 2005; Hinson, 2006) exhibiting similar combinations of zonal wave number, period, and zonal phase speed. However, the period of mode  $d$  (2.0 sols) is shorter than what is typically observed for wave-3 baroclinic eddies (2.2–2.4 sols). A closer comparison with RS results from the preceding year reveals other similarities and differences. The baroclinic eddies in autumn of MY 26 progress through the same sequence of wave numbers as modes  $b$ ,  $c$ , and  $d$  of Table 2 (Hinson, 2006, Table 2), but there are significant year-to-year variations in the amplitudes, the periods, and the timing of the mode transitions. For example, mode  $d$  of MY 27 appears sooner (by  $10^\circ$  of  $L_s$ ) with a larger amplitude (by 70%) and a shorter period (by 10%) than its wave-3 counterpart in MY 26.

The time of each dust storm in Table 1 is marked by a vertical line in Fig. 11. Key properties of the baroclinic eddies are reflected in the characteristics of these regional dust storms. As noted previously, the frontal stage in the first two pairs of storms ( $L_s = 175\text{--}185^\circ$ ) exhibits a wave-2 zonal structure, which matches the zonal wave number of both a prominent baroclinic eddy (mode  $b$ ) and a stationary wave that appear at this time. The 2-sol periodicity of the dust storm sequence in Figs. 5–8 ( $L_s = 224\text{--}226^\circ$ ) conforms to the period of contemporaneous eddy mode  $d$  (2.0 sols), which is distinguished by its large amplitude (294 m) and compact spatial structure ( $s = 3$ ).

Most of the regional dust storms occur after the baroclinic mode transition at  $L_s = 215^\circ$ , when the zonal wave number of the dominant baroclinic eddy shifts from  $s = 1$  (mode  $c$ ) to  $s = 3$  (mode  $d$ ). In addition, the timing of the regional dust storms appears to be correlated with the amplitude of the wave-2 stationary wave in Fig. 11. This suggests that not only baroclinic eddies but also stationary waves play a role in initiating the regional dust storms. We will examine the nature of this interaction more closely in Section 5.4.

### 5.3. Meridional winds

Measurements of  $Z_{610}$  provide valuable information about the meridional winds near the surface, where estimates of wind speeds

**Table 2**  
Characteristics of prominent baroclinic eddies.

Label	$L_s$ ( $^\circ$ )	$\phi$ ( $^\circ$ N)	$s$	$P$ (sols)	$A$ (m)	$u_p$ ( $^\circ$ sol $^{-1}$ )
a	178–186	73	1	9.4	186	38
b	182–190	71	2	2.3	195	79
c	204–212	66	1	6.9	272	52
d	220–228	65	3	2.0	294	59
e	230–238	66	3	2.3	223	51
f	253–261	71	1	6.5	140	56

Note: These results were derived by applying space–time analysis to measurements of  $Z_{610}$  obtained between late summer and winter solstice of MY 27. In the column headings,  $L_s$  is the areocentric longitude of the Sun,  $\phi$  is latitude,  $s$  is the zonal wave number,  $P$  is the period,  $A$  is the amplitude, and  $u_p$  is the zonal phase speed.

are sparse. The 610-Pa pressure level is probably far enough above the ground to decouple the flow from surface friction, at least in the latitude range considered here. In addition, the mean zonal winds are relatively weak at this pressure level (e.g. Banfield et al., 2003, Fig. 3). (They should be comparable to the zonal phase speed of the baroclinic eddies (e.g. Gill, 1982, Section 13.4), or about  $10\text{--}15\text{ m s}^{-1}$  for the eddy modes in Table 2.) Under these conditions, the flow remains near geostrophic balance:

$$v \approx \frac{g}{f_c r_m \cos \phi} \frac{\partial Z}{\partial \lambda}, \quad (5)$$

where  $v$  is the meridional wind speed (positive northward),  $g$  is the acceleration of gravity,  $f_c$  is the Coriolis parameter,  $r_m$  is the radius of Mars, and  $\phi$  is latitude. The derivative is evaluated at constant latitude, pressure, and time. For wave-like eddy modes, such as those described by Eq. (4),  $v$  is proportional to both the amplitude  $A$  and the zonal wave number  $s$ .

Occultations conducted on consecutive orbits yield values of  $Z_{610}$  at fixed latitude but the measurements are not simultaneous. During the interval of 0.08 sols between each pair of observations, the measurement longitude moves westward by about  $29^\circ$  while the baroclinic eddies travel eastward by about  $4^\circ$  (Table 2). The effective zonal separation between the measurements for computing  $\partial Z/\partial \lambda$  is therefore about  $33^\circ$ . Apart from this small correction for eddy motion, the meridional wind speed can be obtained with little difficulty, requiring no other assumptions about the period or zonal wave number of the eddies.

We used finite differences to estimate  $\partial Z/\partial \lambda$  in Eq. (5), which then yields the average value of  $v$  within the longitude interval between adjacent samples. The effect of averaging becomes more serious as  $s$  increases, resulting in an underestimate of the peak winds associated with the wave-3 eddies. In Section 5.4 we will introduce an alternate method for deriving wind speeds that avoids this limitation.

We applied this method of analysis to measurements of  $Z_{610}$  from  $L_s = 140\text{--}270^\circ$  of MY 27, obtaining an estimate of the meridional wind speed for each of about 2000 cases where data are available on successive orbits. These observations can be used to characterize the wind statistics and their dependence on the properties of the baroclinic eddies.

Fig. 12 shows results in the form of a distribution function, defined as the fraction of wind speeds whose magnitude exceeds a given value. The meridional winds are significantly weaker in curve A ( $L_s = 204\text{--}212^\circ$ ) than in curve B ( $L_s = 220\text{--}228^\circ$ ). There is a simple explanation for this, which nonetheless illustrates an important point. The dominant baroclinic eddies in these intervals have similar amplitudes, but the zonal wave number increases from  $s = 1$  in

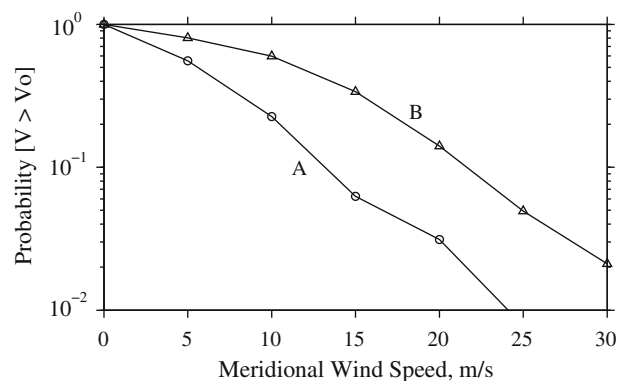


**Fig. 12.** Statistics of meridional winds implied by geostrophic balance at 610 Pa during (A)  $L_s = 204\text{--}212^\circ$  and (B)  $L_s = 220\text{--}228^\circ$ . Each curve shows the fraction of wind samples whose magnitude exceeds the value on the abscissa.

the former to  $s = 3$  in the latter (Table 2), causing proportionate increases in both  $\partial Z/\partial \lambda$  and  $v$ . Hence, transitions among eddy modes with different values of  $s$  impose strong modulation on the intensity of the meridional winds.

We computed distribution functions like those in Fig. 12 for the full set of observations, tabulating the fraction of wind speeds that exceeds  $15 \text{ m s}^{-1}$ , or  $F_{15}$  for short, from within a sliding  $8^\circ$  window of  $L_s$ . This statistic emphasizes winds in the tail of the distribution, which are particularly important because of their potential to raise dust from the surface. The results appear in Fig. 13, which tracks the variations of  $F_{15}$  between late summer and winter solstice of MY 27.

The intensity of the meridional winds, as characterized in Fig. 13, varies strongly with  $L_s$  in response to variations in the amplitude and zonal wave number of the dominant eddy mode. Transitions between eddy modes with different zonal wave numbers are responsible for the most dramatic changes in  $F_{15}$ , such as the rapid increase at  $L_s = 210\text{--}220^\circ$  in the transition from mode  $c$  ( $s = 1$ ) to mode  $d$  ( $s = 3$ ), and the subsequent rapid decrease at  $L_s = 235\text{--}245^\circ$  in the transition from mode  $e$  ( $s = 3$ ) to mode  $f$  ( $s = 1$ ). The strongest winds occur at  $L_s = 220\text{--}230^\circ$  in connection with eddy mode  $d$  ( $s = 3$ ), which produces peak winds that exceed  $30 \text{ m s}^{-1}$  at 610 Pa (curve B of Fig. 12). A secondary peak in  $F_{15}$  appears near  $L_s = 180^\circ$  in connection with eddy mode  $b$  ( $s = 2$ ).

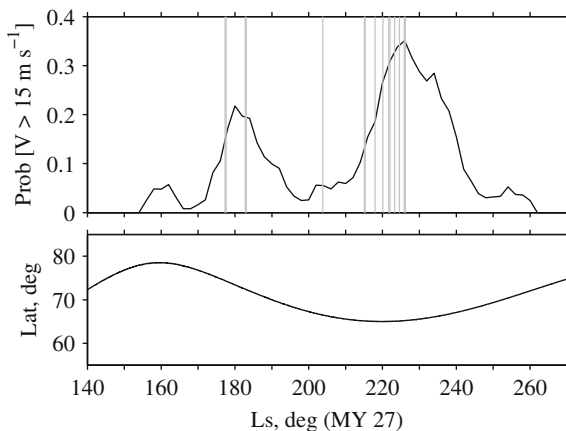
The results in Fig. 13 are undoubtedly influenced by the variations in the latitude of the RS measurements. However, the drift in latitude is very gradual, as shown in the lower panel of Fig. 13, so that the modulation arising from this drift cannot account for the most prominent changes in  $F_{15}$ , which occur on relatively short time scales.

Fig. 13 also compares the seasonal variations of  $F_{15}$  with the timing of the regional dust storms, as listed in Table 1. Most of these dust storms are associated with relatively large values of  $F_{15}$ . This appears to be a direct consequence of the baroclinic mode transitions, which influence the timing of regional dust storms in the northern hemisphere by modulating the intensity of winds near the surface.

Fig. 13 reveals another intriguing pattern. No regional dust storms were observed after the peak in  $F_{15}$  near  $L_s = 226^\circ$ , which suggests a tendency for such storms to occur at times when  $F_{15}$  is rising rather than falling. We will return to this point in Section 6.4.

#### 5.4. The reconstructed waveform

Mode  $d$  is the dominant baroclinic eddy during the interval,  $L_s = 220\text{--}228^\circ$ , when the regional dust storms become particularly



**Fig. 13.** Seasonal variations of meridional winds implied by geostrophic balance at 610 Pa. (top) Fraction of wind samples whose magnitude exceeds  $15 \text{ m s}^{-1}$  from within a sliding  $8^\circ$  window of  $L_s$ . The vertical lines denote the times of the regional dust storms listed in Table 1. (bottom) Latitude of the measurements.

intense. This results in part from the large amplitude and compact spatial structure of this eddy mode. Moreover, the period of this mode is unusually close to 2 sols, and it appears to impose this periodicity on the sequence of regional dust storms shown in Figs. 5–8. We now take a closer look at the behavior of this  $s = 3$  eddy mode and the accompanying  $s = 2$  stationary wave. The results will help explain both the timing and location of the dust storms that occurred within this interval.

Fig. 14 shows the detrended measurements of  $Z_{610}$  during the span of eddy mode  $d$ ,  $L_s = 220\text{--}228^\circ$ . Throughout this interval  $Z_{610}$  oscillates with a well defined frequency and also exhibits a regular pattern of amplitude modulation, including strong positive peaks of about  $+900 \text{ m}$  that recur every 2 sols, corresponding to the period of eddy mode  $d$  (Table 2).

The spectrogram of  $Z_{610}$  in Fig. 11 contains five narrow spectral peaks during  $L_s = 220\text{--}228^\circ$ . Three of these are traveling waves with essentially the same frequency ( $\sigma \approx 0.49 \text{ sol}^{-1}$ ) but different values of zonal wave number ( $s = 1, 2, \text{ and } 3$ ). As noted previously, this is the mathematical signature of baroclinic eddies whose amplitude varies with longitude. These traveling waves are accompanied by two stationary waves ( $\sigma \approx 0$ ) with zonal wave numbers  $s = 1$  and  $2$ . We labeled each spectral peak with an index  $i$  and used the method of analysis described in Section 5.1 to obtain solutions for  $A_i$ ,  $s_i$ ,  $\sigma_i$ , and  $\psi_i$ . We then combined the results into a model for the observed space–time variations of  $Z_{610}$ :

$$Z'' = \sum_{i=1}^5 A_i \cos(s_i \lambda - 2\pi \sigma_i t_u - \psi_i). \quad (6)$$

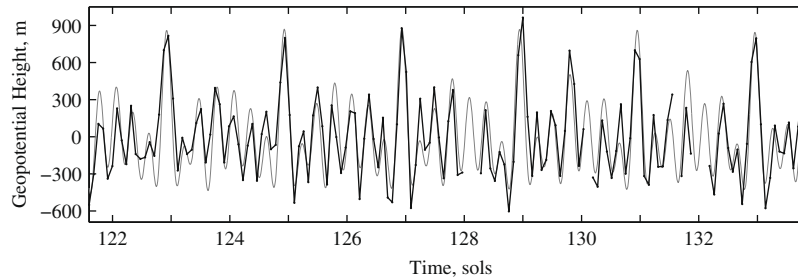
The reconstructed waveform  $Z''$  is a summation over the five main components of the periodogram, with each term taking the form of Eq. (4).

Fig. 14 compares the reconstructed waveform  $Z''$  with the detrended measurements of  $Z_{610}$ . The model reproduces the main features of the data, such as the strong, recurring, positive peaks of  $Z_{610}$ , and it closely tracks the phase of the observed oscillations throughout this 12-sol interval. The agreement between the model and the measurements is particularly good at sols 125–130. Having demonstrated the accuracy of the reconstructed waveform, we can now use it to explore aspects of eddy behavior that were not measured directly.

Fig. 15 shows the reconstructed waveform as it would have appeared in a series of synoptic observations, each at a fixed value of  $t_u$ . The figure includes results at eight uniform time steps that span the 2-sol period of the traveling waves. The composite waveform has a distinct wave-3 character, corresponding to the zonal wave number of the dominant spectral feature (eddy mode  $d$ ), but its amplitude varies strongly with longitude.

The dynamics in Fig. 15 appear to be coupled with Alba Mons in two respects. First, the baroclinic eddies achieve their largest amplitude at the longitude of this topographic feature ( $250^\circ\text{E}$ ), where the peak-to-trough variations in amplitude reach  $1200 \text{ m}$ . Second, both stationary waves, whose amplitudes are about  $130 \text{ m}$  at  $s = 1$  and  $170 \text{ m}$  at  $s = 2$ , have ridges in geopotential height near  $250^\circ\text{E}$ , as shown by the dashed curve in Fig. 15. The alignment of these stationary waves with Alba Mons accounts for the large asymmetry between the peaks ( $+900 \text{ m}$ ) and the troughs ( $-300 \text{ m}$ ) of  $Z''$  at this longitude.

We computed the winds implied by geostrophic balance by applying Eq. (5) to each of the reconstructed waveforms in Fig. 15. The results appear in Fig. 16. As with the geopotential field, the magnitude of the meridional winds varies considerably with longitude. The peak-to-trough variations of wind speed range from a minimum of about  $25 \text{ m s}^{-1}$  at  $120^\circ\text{E}$ , north of Utopia, to a maximum of about  $50 \text{ m s}^{-1}$  at  $250^\circ\text{E}$ , north of Alba Mons. The circulation around Alba Mons is also markedly asymmetric. In northern



**Fig. 14.** Space-time variations in geopotential height at 610 Pa during  $L_s = 220\text{--}228^\circ$  of MY 27. The dots denote samples of  $Z_{610}$  at  $65^\circ\text{N}$  obtained from the 147 occultation experiments conducted within this 12-sol interval. Dark lines connect measurements from consecutive orbits. The light line shows the waveform reconstructed from spectral analysis, as represented by Eq. (6).

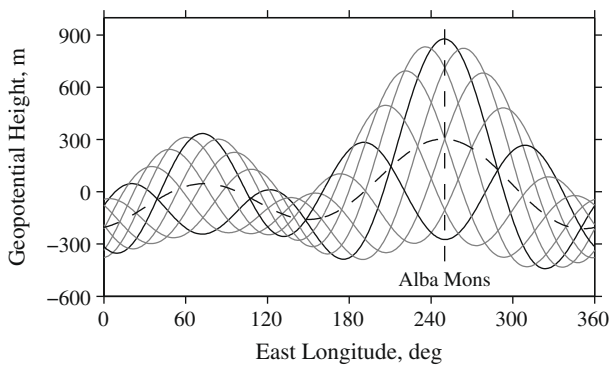


**Fig. 15.** Zonal structure and time evolution of geopotential height (610 Pa) at  $65^\circ\text{N}$  during  $L_s = 220\text{--}228^\circ$  of MY 27. Each solid curve shows a snapshot at fixed  $t_i$  of the full waveform reconstructed through spectral analysis, as represented by Eq. (6). The family of curves tracks the eastward motion of the waveform at eight values of  $t_i$  spread uniformly across the 2-sol period of the dominant eddy mode. The dashed curve shows the contribution by stationary waves with  $s = 1$  and 2. The dashed vertical line marks the longitude of Alba Mons.

Acidalia (near  $310^\circ\text{E}$ ), the peak southward winds ( $-30\text{ m s}^{-1}$ ) are about twice as strong as the peak northward winds ( $+15\text{ m s}^{-1}$ ). The reverse is true in northern Arcadia (near  $200^\circ\text{E}$ ), where the meridional winds have a comparable northward bias.

This asymmetry in the wind field is a consequence of the  $s = 2$  stationary wave, which imposes a steady, clockwise (anticyclonic) bias to the circulation around Alba Mons, as shown by the dashed curve in Fig. 16. This reinforces the circulation that occurs when a geopotential ridge of the eastward-traveling wave is aligned with

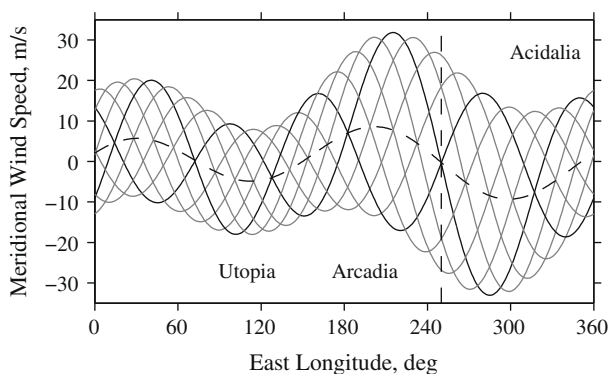


**Fig. 16.** The meridional winds implied by geostrophic balance at  $65^\circ\text{N}$  during  $L_s = 220\text{--}228^\circ$  of MY 27. Each solid curve was obtained by applying Eq. (5) to one of the reconstructed waveforms of geopotential height (610 Pa) in Fig. 15. Positive winds are northward. The dashed curve shows the contribution from stationary waves, which is dominated by the  $s = 2$  component. The dashed vertical line marks the longitude of Alba Mons.

Alba Mons, producing intense winds moving northward from Arcadia and southward toward Acidalia. Conversely, the stationary wave inhibits the counterclockwise (cyclonic) circulation that occurs about 1 sol later when the ridge is replaced by a trough. These two situations are depicted by the pairs of dark solid curves in Figs. 15 and 16.

These results offer a plausible explanation for the uneven spatial distribution of the regional dust storms, including those depicted in Figs. 5–8. Intense southward winds are conducive to the occurrence of these dust storms, particularly in their flushing stage. In this regard the preponderance of flushing dust storms in Acidalia during  $L_s = 220\text{--}228^\circ$  (Table 1) correlates well with the concentration of strong southward winds at longitudes of  $250\text{--}320^\circ\text{E}$ , as shown in Fig. 16. The peak southward winds in Arcadia and Utopia are comparatively weak. Hence, the location of these regional dust storms appears to be controlled in part by the combined effects of a wave-2 stationary wave and storm-zone modulation of the baroclinic eddies.

Finally, we compared the timing of the dust storms with the phase of the oscillations in geopotential height. A cyclic pattern of regional dust storms occurred in Acidalia at 2-sol intervals during  $L_s = 222\text{--}226^\circ$ , as listed in Table 1 and shown in Figs. 5–8. The flushing stage of each storm coincided with the arrival of a geopotential ridge at the longitude of Alba Mons, as cold dense air surged southward toward Acidalia. These eddy winds appear to provide an important impetus to the flushing stage of the dust storm.

## 6. Discussion

We have characterized important aspects of martian meteorology using a combination of radio occultation data and MDGMs, both obtained with MGS. We used the former to characterize the behavior of baroclinic eddies and stationary waves at high northern latitudes between midsummer and winter solstice of MY 27 (January–August 2005). No other atmospheric sounder was in operation at this time. We surveyed contemporaneous MDGMs and assembled a catalog of regional dust storms. Our investigation has identified key factors that influence the timing and location of distinctive flushing dust storms that occur in the major topographic basins of the northern hemisphere. These include baroclinic mode transitions, storm zones, and stationary waves. The following sections discuss selected aspects of our results with emphasis on their relationship to previous work.

### 6.1. The midautumn dust storm season

The flushing dust storms and baroclinic eddies in autumn of MY 27 resemble their counterparts of MY 24 in several key respects. First, the most vigorous flushing storms in autumn of MY 24 occurred at  $L_s = 221\text{--}225^\circ$  in Acidalia (e.g. Cantor et al., 2001, Section

6.6), which coincides in both season and location with the most intense events reported here. Second, this sequence of flushing storms in MY 24 appeared to be triggered by the abrupt intensification at about  $L_s = 220^\circ$  of a wave-3 baroclinic eddy with a period of 2.2 sols. The basic properties of this eddy mode were first discussed by Banfield et al. (2004, Section 4.3.1) and its association with the flushing dust storms of MY 24 was first reported by Wang et al. (2005, Fig. 12). Its characteristics and time of appearance are similar to eddy mode *d* of MY 27 (Table 2). In both years a series of vigorous flushing dust storms follows immediately after the transition to a wave-3 baroclinic eddy mode. This comparison highlights a pattern of autumn weather that may recur in a significant fraction of martian years.

Observations by the MOC during autumn of MY 25 were dominated by a major, planet-encircling dust storm that began near  $L_s = 185^\circ$  (e.g. Cantor, 2007). By  $L_s = 197^\circ$ , the planet was enshrouded in a dust cloud that largely obscured the surface. The global enhancement of dust opacity persisted into early winter. The behavior of the atmosphere throughout this period diverges significantly from what was observed in autumn of MY 27, and further comparison is beyond the scope of this discussion. However, we note that the catalog of frontal and flushing dust storms compiled by Wang et al. (2005) and Wang (2007) includes observations from autumn of MY 25, while the contemporaneous baroclinic eddies are discussed by Banfield et al. (2004).

The most vigorous flushing dust storms in autumn of MY 26 appeared at about  $L_s = 210\text{--}215^\circ$  in Utopia, as described by Cantor (2007, Fig. 19) and Wang (2007, Fig. 1). These events differ in both time and location from their counterparts in MY 27. Nonetheless, there are important similarities in the general patterns of behavior in these two years. For example, the wave-1 baroclinic eddy is the dominant mode during  $L_s = 215\text{--}225^\circ$  of MY 26 (e.g. Hinson, 2006, Fig. 4 and Table 2) and  $L_s = 205\text{--}215^\circ$  of MY 27 (Fig. 11 and Table 2). (Their periods are 5.9 sols in MY 26 and 6.9 sols in MY 27.) Flushing dust storms are conspicuously absent from these intervals in both MY 26 (Wang, 2007, Fig. 1) and MY 27 (Fig. 11 and Table 1). Although the transition to a dominant wave-1 eddy mode occurs at different times in the two years, the resulting suppression of flushing dust storms is the same. Hence, the differences between the autumn weather in MY 26 and 27 are related to interannual variations in the timing of the baroclinic mode transitions.

## 6.2. Storm zones

On the basis of pre-MGS numerical simulations, Hollingsworth et al. (1996, 1997) predicted that the amplitude of eastward-traveling baroclinic eddies should vary strongly with longitude at high northern latitudes. The existence of such storm zones in the northern hemisphere was confirmed by Banfield et al. (2004, Section 5 and Fig. 20) through analysis of temperature measurements by the MGS TES. In subsequent analysis of the same data, Wang et al. (2005) further characterized the storm zones and documented their influence on the timing and location of flushing dust storms.

The results reported here reveal another important property of the storm zones of the northern hemisphere. As noted previously, a storm zone can be identified in measurements of  $Z_{610}$  by its distinctive spectral signature, which consists of several narrow peaks with the same period but different zonal wave numbers. The spectrogram in Fig. 11 exhibits this type of behavior only during  $L_s = 220\text{--}240^\circ$ , the period dominated by wave-3 baroclinic eddies (modes *d* and *e*). Hence, this zonal modulation of eddy amplitude appears to arise from a scale-dependent process that operates most effectively for wave-3 eddy modes.

## 6.3. The $s = 2$ stationary wave

Basic properties of the wave-2 stationary Rossby wave are known from previous investigations. Although its amplitude changes significantly with season, its zonal phase remains essentially constant (e.g. Banfield et al., 2003, Fig. 10). The geopotential field at high northern latitudes conforms to the local zonal variations of surface topography, with persistent maxima in geopotential height appearing at longitudes near  $60^\circ\text{E}$  and  $240^\circ\text{E}$  throughout northern autumn and winter (e.g. Hinson, 2006), consistent with the results shown here in Fig. 15.

This stationary wave imposes significant wave-2 zonal modulation on the structure of northern polar hood clouds (e.g. Wang and Ingersoll, 2002, Fig. 2). The boundary of the polar hood extends farther southward in Acidalia and Utopia than at other longitudes, and this pattern persists throughout northern autumn and winter.

The wave-2 stationary wave also has a distinctive “equivalent barotropic” vertical structure. Its zonal phase at high latitudes is essentially independent of height at pressures greater than 10 Pa, with no appreciable eastward or westward tilt, as noted by Banfield et al. (2003, Fig. 10). As a direct consequence, the amplitude in geopotential height grows steadily with increasing altitude (e.g. Hinson et al., 2003, Fig. 7). For the RS observations considered in Section 5.4 ( $L_s = 220\text{--}228^\circ$  of MY 27 at  $65^\circ\text{N}$ ), its amplitude increases from about 170 m at 610 Pa to about 740 m at 30 Pa with no appreciable change in zonal phase.

The results reported here extend our understanding of the  $s = 2$  stationary wave to include its climatic significance. This arises primarily through its influence on the location of regional dust storms, as discussed in Section 5.4. More generally, flushing dust storms tend to occur when the amplitude of the wave-2 stationary wave is relatively large, as noted in Section 5.2 and shown in Fig. 11.

## 6.4. The cessation of flushing dust storms

No regional dust storms were observed in the northern hemisphere after about  $L_s = 226^\circ$  of MY 27. We are not sure why this happened, and we now offer several possible explanations.

Fig. 13 shows that regional dust storms in the northern hemisphere are associated with relatively large values of  $F_{15}$ , a statistical measure of the strength of the meridional winds at 610 Pa. However, there is a striking asymmetry in this correlation. Ten flushing storms occurred during  $L_s = 215\text{--}226^\circ$  as  $F_{15}$  was rising steadily to its peak value, but this type of dust storm was absent from the interval that followed,  $L_s = 226\text{--}240^\circ$ , when  $F_{15}$  was decreasing through the same range of values. This type of behavior might reflect the cumulative effect of the flushing storms on the surface reservoirs of dust. By removing the dust that is easiest to lift, each flushing storm might raise the wind threshold required for dust lifting in subsequent events. The cycle of frontal and flushing storms that recurs in Acidalia during  $L_s = 221\text{--}226^\circ$  could be susceptible to this process. (More generally, this phenomenon may contribute to the interannual variability of the martian dust cycle, Pankine and Ingersoll, 2002, 2004.)

The demise of the flushing dust storms in midautumn may also be related to seasonal deposition of  $\text{CO}_2$  ice at high northern latitudes. Condensing  $\text{CO}_2$  could scavenge dust from the atmosphere and blanket surface reservoirs of dust at key locations, thereby inhibiting the flushing storms. These processes seem relevant in light of the results in Fig. 9, which show that the oscillations in  $T_{610}$  at high northern latitudes rarely reach saturation prior to  $L_s = 220^\circ$  but do so routinely after  $L_s = 230^\circ$ .

According to numerical simulations (Wang et al., 2003; Wilson et al., 2006), flushing storms occur preferentially during daytime, within the range of local times when their southward motion is

reinforced by the diurnally-varying, near-surface winds that arise from thermal tides and topographic circulations. Baroclinic eddies are most likely to initiate a flushing dust storm when their zonal phase results in effective coupling between the “frontal” and “tidal” wind fields. Mode *d* apparently satisfies this condition and remains locked in zonal phase to a configuration that produces a repetitive sequence of vigorous flushing dust storms in Acidalia. In this regard, the end of the flushing dust storms may be due in part to the transition from mode *d* to mode *e* at about  $L_s = 230^\circ$ , which disrupts the synchronization between the frontal and tidal wind fields. With the increase in period from 2.0 sols (mode *d*) to 2.3 sols (mode *e*), favorable alignments of frontal and tidal winds occur less frequently, resulting in fewer opportunities for flushing dust storms.

The end of the flushing storms also coincides with a significant change in the global state of the atmosphere. The Thermal Emission Imaging System (THEMIS) on Mars Odyssey observed abrupt increases in the zonal-mean dust opacity and atmospheric temperature near  $L_s = 225^\circ$  of MY 27 (Smith, 2009, Fig. 6), which arose in part from the regional dust storms described in Section 3 (Cantor, 2007, Section 5.7). This type of planet-encircling haze can modify the wind field near the surface by increasing the amplitude of the semidiurnal tide (e.g. Leovy and Zurek, 1979; Leovy, 1981; Zurek and Leovy, 1981; Leovy et al., 1985). Dust-storm amplification of the semidiurnal tide results in dramatic changes in the magnitude and direction of near-surface winds and their variations with local time (e.g. Leovy and Zurek, 1979, Fig. 2), which could in principle inhibit the occurrence of flushing dust storms.

## Acknowledgments

Funding for this research was provided by NASA under Grants NNX08AL24G (Hinson) and NNX07AR10G (Wang) of the Mars Data Analysis Program. We relied on NASA's Navigation and Ancillary Information Facility (Acton, 1996) in various stages of data analysis. In preparing the manuscript we made use of the SAO/NASA Astrophysics Data System (<http://adswww.harvard.edu/>) and an Icarus LaTeX template created by R.A. Beyer, D.P. O'Brien, P. Withers, and G. Bart (<http://rossbeyer.net/software/>).

## References

- Acton, C.H., 1996. Ancillary data services of NASA's navigation and ancillary information facility. *Planet. Space Sci.* 44, 65–70.
- Banfield, D., Conrath, B.J., Smith, M.D., Christensen, P.R., Wilson, R.J., 2003. Forced waves in the martian atmosphere from MGS TES nadir data. *Icarus* 161, 319–345. doi:10.1016/S0019-1035(02)00044-1.
- Banfield, D., Conrath, B.J., Gierasch, P.J., Wilson, R.J., Smith, M.D., 2004. Traveling waves in the martian atmosphere from MGS TES nadir data. *Icarus* 170, 365–403. doi:10.1016/j.icarus.2004.03.015.
- Barnes, J.R., 1980. Time spectral analysis of midlatitude disturbances in the martian atmosphere. *J. Atmos. Sci.* 37, 2002–2015. doi:10.1175/1520-046(1980)037.
- Barnes, J.R., 1981. Midlatitude disturbances in the martian atmosphere – A second Mars year. *J. Atmos. Sci.* 38, 225–234. doi:10.1175/1520-046(1981)038.
- Barnes, J.R., 1984. Linear baroclinic instability in the martian atmosphere. *J. Atmos. Sci.* 41, 1536–1550. doi:10.1175/1520-046(1984)041.
- Basu, S., Wilson, J., Richardson, M., Ingersoll, A., 2006. Simulation of spontaneous and variable global dust storms with the GFDL Mars GCM. *J. Geophys. Res. (Planets)* 111, E09004. doi:10.1029/2005JEO02660.
- Cantor, B.A., 2007. MOC observations of the 2001 Mars planet-encircling dust storm. *Icarus* 186, 60–96. doi:10.1016/j.icarus.2006.08.019.
- Cantor, B.A., James, P.B., Caplinger, M., Wolff, M.J., 2001. Martian dust storms: 1999 Mars Orbiter Camera observations. *J. Geophys. Res. (Planets)* 106 (E10), 23653–23688. doi:10.1029/2000JEO01310.
- Cantor, B.A., Kanak, K.M., Edgett, K.S., 2006. Mars Orbiter Camera observations of martian dust devils and their tracks (September 1997 to January 2006) and evaluation of theoretical vortex models. *J. Geophys. Res. (Planets)* 111, E12002. doi:10.1029/2006JEO02700.
- Chapman, W.A., Cross, M.J., Flower, D.A., Peckham, G.E., Smith, S.D., 1974. A spectral analysis of global atmospheric temperature fields observed by the selective chopper radiometer on the Nimbus 4 satellite during the year 1970–1. *Roy. Soc. Lond. Proc. Ser. A* 338, 57–76.
- Clancy, R.T., Sandor, B.J., Wolff, M.J., Christensen, P.R., Smith, M.D., Pearl, J.C., Conrath, B.J., Wilson, R.J., 2000. An intercomparison of ground-based millimeter, MGS TES, and Viking atmospheric temperature measurements: Seasonal and interannual variability of temperatures and dust loading in the global Mars atmosphere. *J. Geophys. Res. (Planets)* 105 (E4), 9553–9572. doi:10.1029/1999JEO01089.
- Collins, M., Lewis, S.R., Read, P.L., Hourdin, F., 1996. Baroclinic wave transitions in the martian atmosphere. *Icarus* 120, 344–357. doi:10.1006/icar.1996.0055.
- Conrath, B.J., 1981. Planetary-scale wave structure in the martian atmosphere. *Icarus* 48, 246–255. doi:10.1016/0019-1035(81)90107-X.
- Gill, A.E., 1982. *Atmosphere–Ocean Dynamics*. Academic Press, San Diego.
- Hinson, D.P., 2006. Radio occultation measurements of transient eddies in the northern hemisphere of Mars. *J. Geophys. Res. (Planets)* 111, E05002. doi:10.1029/2005JEO02612.
- Hinson, D.P., Wang, H., 2008. Baroclinic eddies and dust storms during autumn of MY 27. In: *Third International Workshop on the Mars Atmosphere: Modeling and Observations*, held 10–13 November 2008 in Williamsburg, VA (LPI Contribution No. 1447: 9019).
- Hinson, D.P., Wilson, R.J., 2002. Transient eddies in the southern hemisphere of Mars. *Geophys. Res. Lett.* 29 (7), 1154. doi:10.1029/2001GL014103.
- Hinson, D.P., Wilson, R.J., 2004. Temperature inversions, thermal tides, and water ice clouds in the martian tropics. *J. Geophys. Res. (Planets)* 109, E01002. doi:10.1029/2003JEO02129.
- Hinson, D.P., Simpson, R.A., Twicken, J.D., Tyler, G.L., Flasar, F.M., 1999. Initial results from radio occultation measurements with Mars Global Surveyor. *J. Geophys. Res. (Planets)* 104 (E11), 26997–27012. doi:10.1029/1999JEO01069.
- Hinson, D.P., Wilson, R.J., Smith, M.D., Conrath, B.J., 2003. Stationary planetary waves in the atmosphere of Mars during southern winter. *J. Geophys. Res. (Planets)* 108 (E1), 5004. doi:10.1029/2002JEO01949.
- Hinson, D.P., Pätzold, M., Wilson, R.J., Häusler, B., Tellmann, S., Tyler, G.L., 2008. Radio occultation measurements and MCGM simulations of Kelvin waves on Mars. *Icarus* 193, 125–138. doi:10.1016/j.icarus.2007.09.009.
- Hollingsworth, J.L., Haberle, R.M., Barnes, J.R., Bridger, A.F.C., Pollack, J.B., Lee, H., Schaeffer, J., 1996. Orographic control of storm zones on Mars. *Nature* 380, 413–416. doi:10.1038/380413a0.
- Hollingsworth, J.L., Haberle, R.M., Schaeffer, J., 1997. Seasonal variations of storm zones on Mars. *Adv. Space Res.* 19 (8), 1237–1240. doi:10.1016/S0273-1177(97)00275-5.
- James, P.B., 1985. Martian local dust storms. In: Hunt, G.E. (Ed.), *Recent Advances in Planetary Meteorology*. Cambridge University Press, New York, pp. 85–99.
- Lait, L.R., Stanford, J.L., 1988. Applications of asymptotic space–time Fourier transform methods to scanning satellite measurements. *J. Atmos. Sci.* 45, 3784–3799.
- Leovy, C.B., 1979. Martian meteorology. *Annu. Rev. Astron. Astrophys.* 17, 387–413. doi:10.1146/annurev.aa.17.090179.002131.
- Leovy, C.B., 1981. Observations of martian tides over two annual cycles. *J. Atmos. Sci.* 38, 30–39.
- Leovy, C.B., Zurek, R.W., 1979. Thermal tides and martian dust storms – Direct evidence for coupling. *J. Geophys. Res.* 84, 2956–2968. doi:10.1029/JB084iB06p02956.
- Leovy, C.B., Tillman, J.E., Guest, W.R., Barnes, J.R., 1985. Interannual variability of martian weather. In: Hunt, G.E. (Ed.), *Recent Advances in Planetary Meteorology*. Cambridge University Press, New York, pp. 69–84.
- Liu, J., Richardson, M.I., Wilson, R.J., 2003. An assessment of the global, seasonal, and interannual spacecraft record of martian climate in the thermal infrared. *J. Geophys. Res. (Planets)* 108 (E8), 5089. doi:10.1029/2002JEO01921.
- Malin, M.C., Danielson, G.E., Ingersoll, A.P., Masursky, H., Veverka, J., Ravine, M.A., Soulanille, T.A., 1992. Mars observer camera. *J. Geophys. Res. (Planets)* 97 (E5), 7699–7718.
- Pankine, A.A., Ingersoll, A.P., 2002. Interannual variability of martian global dust storms. *Icarus* 155, 299–323. doi:10.1006/icar.2001.6757.
- Pankine, A.A., Ingersoll, A.P., 2004. Interannual variability of Mars global dust storms: An example of self-organized criticality? *Icarus* 170, 514–518. doi:10.1016/j.icarus.2004.04.006.
- Press, W.H., Teukolsky, S.A., 1988. Search algorithm for weak periodic signals in unevenly spaced data. *Comput. Phys.* 2 (6), 77–82.
- Ryan, J.A., Henry, R.M., Hess, S.L., Leovy, C.B., Tillman, J.E., Walcek, C., 1978. Mars meteorology – Three seasons at the surface. *Geophys. Res. Lett.* 5, 715–718. doi:10.1029/GL005i008p00715.
- Salby, M.L., 1982. Sampling theory for asymptotic satellite observations. Part I: Space-time spectra, resolution, and aliasing. *J. Atmos. Sci.* 39, 2577–2600.
- Smith, M.D., 2004. Interannual variability in TES atmospheric observations of Mars during 1999–2003. *Icarus* 167, 148–165. doi:10.1016/j.icarus.2003.09.010.
- Smith, M.D., 2009. THEMIS observations of Mars aerosol optical depth from 2002–2008. *Icarus* 202, 444–452.
- Smith, D.E., and 23 colleagues, 2001. Mars Orbiter Laser Altimeter: Experiment summary after the first year of global mapping of Mars. *J. Geophys. Res. (Planets)* 106, 23689–23722. doi:10.1029/2000JEO01364.
- Strausberg, M.J., Wang, H., Richardson, M.I., Ewald, S.P., Toigo, A.D., 2005. Observations of the initiation and evolution of the 2001 Mars global dust storm. *J. Geophys. Res. (Planets)* 110 (E9), E02006. doi:10.1029/2004JEO02361.
- Wang, H., 2007. Dust storms originating in the northern hemisphere during the third mapping year of Mars Global Surveyor. *Icarus* 189, 325–343. doi:10.1016/j.icarus.2007.01.014.

- Wang, H., Ingersoll, A.P., 2002. Martian clouds observed by Mars Global Surveyor Mars Orbiter Camera. *J. Geophys. Res. (Planets)* 107 (E10), 5078. doi:10.1029/2001JE001815.
- Wang, H., Richardson, M.I., Wilson, R.J., Ingersoll, A.P., Toigo, A.D., Zurek, R.W., 2003. Cyclones, tides and the origin of a cross-equatorial dust storm on Mars. *Geophys. Res. Lett.* 30 (9), 1488. doi:10.1029/2002GL016828.
- Wang, H., Zurek, R.W., Richardson, M.I., 2005. Relationship between frontal dust storms and transient eddy activity in the northern hemisphere of Mars as observed by Mars Global Surveyor. *J. Geophys. Res. (Planets)* 110 (E9), E07005. doi:10.1029/2005JE002423.
- Wilson, R.J., Banfield, D., Conrath, B.J., Smith, M.D., 2002. Traveling waves in the northern hemisphere of Mars. *Geophys. Res. Lett.* 29 (14), 1684. doi:10.1029/2002GL014866.
- Wilson, R.J., Hinson, D., Smith, M.D., 2006. GCM simulations of transient eddies and frontal systems in the martian atmosphere. In: Forget, F., Lopez-Valverde, M.A., Desjean, M.C., Huot, J.P., Lefevre, F., Lebonnois, S., Lewis, S.R., Millour, E., Read, P.L., Wilson, R.J. (Eds.), *Mars Atmosphere Modelling and Observations*, pp. 154–158.
- Wu, D.L., Hays, P.B., Skinner, W.R., 1995. A least squares method for spectral analysis of space–time series. *J. Atmos. Sci.* 52, 3501–3511. doi:10.1175/1520-0469(1995)052.
- Zurek, R.W., Leovy, C.B., 1981. Thermal tides in the dusty martian atmosphere – A verification of theory. *Science* 213, 437–439.
- Zurek, R.W., Barnes, J.R., Haberle, R.M., Pollack, J.B., Tillman, J.E., Leovy, C.B., 1992. Dynamics of the atmosphere of Mars. In: Kieffer, H.H., Jakosky, B.M., Snyder, C.W., Matthews, M.S. (Eds.), *Mars*. University of Arizona Press, Tucson, pp. 835–933.